Measurement report: Diurnal variations of brown carbon during two distinct seasons in a megacity in Northeast China

Yuan Cheng[1], Xu-bing Cao[1], Jiu-meng Liu[1,*], Ying-jie Zhong[1], Qin-qin Yu[1], Qiang Zhang[2] and Ke-bin He[3]

[1] State Key Laboratory of Urban Water Resource and Environment, School of Environment, Harbin Institute of Technology, Harbin 150090, China

[2] Ministry of Education Key Laboratory for Earth System Modeling, Department of Earth System Science, Tsinghua University, Beijing 100084, China

[3] State Key Joint Laboratory of Environment Simulation and Pollution Control, School of Environment, Tsinghua University, Beijing 100084, China

[*]Corresponding author. Jiu-meng Liu (jiumengliu@hit.edu.cn).

Abstract

Brown carbon (BrC) represents an important target for the "win-win" strategy of mitigating climate change and improving air quality. However, estimating co-benefits of BrC control remains difficult for China, partially because current measurement results are insufficient to represent the highly variable emission sources and meteorological conditions across different regions. In this study, we investigated, for the first time, the diurnal variations of BrC during two distinct seasons in a megacity in Northeast China. The winter campaign conducted in January of 2021 was characterized by low temperatures rarely seen in other Chinese megacities (down to about –20 °C). The mass absorption efficiencies of BrC at 365 nm (MAE_{365}) were found to be ~10% higher at night. The variations of MAE_{365} could not be explained by the influence of residential biomass burning emissions or secondary aerosol formation, but were strongly associated with the changes of a diagnostic ratio for the relative importance of coal combustion and vehicle emissions ($R_{S/N}$). Given that most coal combustion activities were uninterruptible, the higher nighttime MAE_{365} in winter were attributed primarily to increased emissions from heavy-duty diesel trucks. The spring

campaign conducted in April of 2021 was characterized by frequent occurrences of agricultural fires, as supported by the intensive fire hotspots detected around Harbin and the more-than-doubled levoglucosan to organic carbon ratios (LG/OC) compared to winter campaign. In spring, MAE_{365} depended little on $R_{S/N}$ but exhibited a strong positive correlation with LG/OC, suggesting open burning emissions as the dominant influencing factor for BrC's light absorption capacity. MAE_{365} were ~70% higher at night for the spring campaign, pointing to the prevalence of nighttime agricultural fires, which were presumably in response to local bans on open burning. It is noteworthy that the agricultural fire emissions resulted in distinct peak at ~365 nm for the light absorption spectra of BrC, and candidates for the compounds at play were inferred to be aromatic species with nitro-functional groups. The presence of the ~365 nm peak complicated the determination of absorption Ångström exponents for the agricultural fire-impacted samples. In addition, the ~365 nm peak became much less significant during the day, likely due to photo-bleaching of the relevant chromophores.

1. Introduction

Light-absorbing organic carbon, i.e., brown carbon (BrC), exerts important yet poorly understood effects on climate and the environment (Brown et al., 2018; Zeng et al., 2020; Sand et al., 2021). As a mixture of numerous organic compounds from both primary emissions and secondary formation, BrC exhibits extreme complexity in spectroscopy, composition and evolution (Laskin et al., 2015; Brege et al., 2021; Washenfelder et al., 2022). Measurement techniques for BrC absorption mainly fell into two categories, including solvent extraction followed by light absorption spectrum measurement (Chen and Bond, 2010; Hecobian et al., 2010) and apportionment of total aerosol absorption to the contributions from black carbon and BrC (Yang et al., 2009; Lack et al., 2012). So far, consistency between BrC results from these two types of approaches has not been addressed, with variable relationships, either linear or non-linear, and unclear influencing factors (Kumar et al., 2018; Zeng et al., 2022). This inconsistency introduced substantial difficulties to the integration of BrC measurement results across studies and regions (Wang et al., 2022), which is essential for unfolding the links between BrC sources and optical properties. In addition, efforts were also made to explain BrC absorption on a molecular level. Several techniques were shown to be powerful, such as electrospray ionization Fourier transform ion cyclotron resonance mass spectrometry (ESI FT-ICR MS; Wozniak et al., 2008; Jiang et al., 2021; Zeng et al., 2021), high performance liquid chromatography coupled with high resolution mass spectrometry (HPLC/HRMS; Lin et al., 2018; Huang et al., 2022; Xu et al., 2022), and two-dimensional gas chromatography with time of flight mass spectrometer (GC×GC-ToF-MS; Huo et al., 2021). These techniques were more frequently applied to laboratory-generated primary or secondary BrC (e.g., Lin et al., 2015), which usually had less complex composition than ambient BrC and thus showed

relatively high fraction of resolvable chromophores, e.g., up to ~85% for those emitted by biomass burning (Huang et al., 2022).

The absorbing nature of BrC makes it a non-negligible contributor to positive radiative forcing (Saleh, 2020), while the considerable contribution of organic aerosol to fine particulate matter ($PM_{2.5}$) makes BrC an important source of air pollution (Wang et al., 2019). Consequently, BrC represents a key species for the "win-win" strategy of mitigating climate change and improving air quality. Given the highly variable emission sources and meteorological conditions across different regions in China, field observational results on BrC are far from being enough to constrain air quality and climate models, limiting the ability to evaluate the co-benefits of BrC control. In this study, we focused on a largely unexplored city cluster, the Harbin-Changchun (HC) metropolitan area in Northeast China. Compared to other regions with intensive studies of BrC as well as other air pollutants (e.g., the North China Plain), HC was characterized by extremely cold winter and strong impacts of biomass burning on top of other anthropogenic emissions (e.g., from coal combustion). The first feature was related to the relatively high latitudes of HC. For example, as the northernmost megacity in China, Harbin has an average temperature of about –20°C in January, significantly lower than that of Beijing (~0 ℃). The second feature was related to the massive agricultural sector in HC. Until recently, open burning was still an irreplaceable approach for the disposal of crop residues in this region, presumably because the amount of agricultural wastes was too huge for the capacity of sustainable use. The agricultural fires frequently resulted in heavily-polluted episodes with high $PM_{2.5}$ concentrations rarely encountered in other Chinese megacities (e.g., hourly-average of ~1000 $\mu g/m^3$ in Harbin; Li et al., 2019). These two features highlighted the uniqueness of HC for haze studies in China.

This measurement report, for the first time, presented field observational results on the diurnal variations of BrC during two distinct seasons, i.e., a frigid winter and an agricultural fire-impacted spring, in the central city of HC. Drivers for the diurnal variations were discussed based on indicators of various sources. Particularly, the agricultural fires were found to result in unique absorption spectra of brown carbon. This study provided implications for parameterization of BrC in climate models.

2. Methods

2.1 Field sampling

Daytime and nighttime $PM_{2.5}$ samples were collected on the campus of Harbin Institute of Technology (HIT) during winter and spring of 2021. HIT was surrounded by residential and commercial areas, without major industrial sources nearby, and thus represented a typical urban site. The sampling was done by a mass flow controlled high-volume sampler (TE-6070BLX-2.5-HVS; Tisch Environmental, Inc., OH, USA), which was operated at a flow rate of 1.13 m^3/min using pre-baked quartz-fiber filters (8″ × 10″, 2500 QAT-UP; Pall Corporation, NY, USA). To avoid rush hours and considering the relatively early sunset time in winter (~16:00–17:00), daytime and nighttime samples were collected from 9:00 to 16:00 and from 21:00 to 5:00 of the next day, respectively. The winter campaign covered the entire January of 2021, and the spring campaign was conducted during 10–30 April, 2021.

2.2 Laboratory analysis

Two punches with diameters of 20 mm were taken from each sample, combined and then extracted by deionized water. The water extract was analyzed using a Dionex ion chromatography system (ICS-5000$^+$; Thermo Fisher Scientific Inc., MA, USA). Levoglucosan, an organic tracer for

105 biomass burning, was determined by the high-performance anion-exchange chromatography
106 coupled to pulsed amperometric detection (HPAEC-PAD) method (Engling et al., 2006; Yttri et al.,
107 2015). Inorganic ions such as nitrate, sulfate, chloride, ammonium and potassium were also
108 measured. Linear regression of the total cation concentration on that of total anion (both in $\mu eq/m^3$)
109 led to a slope of 1.14 ± 0.01 (intercept was set as zero; $r = 0.99$), indicating a neutralized feature of
110 the Harbin aerosols.

111 Two punches with diameters of 47 mm were taken from each sample and used to determine
112 carbon fractions. Following the method developed by Chen and Bond (2010) and refined by Cheng
113 et al. (2016), one punch was directly measured for organic carbon and elemental carbon, while the
114 other punch was immersed in methanol (HPLC grade; Fisher Scientific Company L.L.C., NJ, USA)
115 for an hour without stirring or sonication, dried in air for another hour, and then analyzed. Both
116 punches were measured by a Thermal/Optical Carbon Analyzer (DRI-2001; Atmoslytic Inc., CA,
117 USA), which was operated with two commonly-used temperature protocols (i.e., IMPROVE-A and
118 NIOSH) and transmittance charring correction. The difference of total carbon (TC) concentrations
119 between the untreated and extracted punches ($TC_{untreated} - TC_{extracted}$) was used to represent the
120 amount of organic carbon that is soluble in methanol (MSOC). Given that the TC measurement was
121 independent of the temperature protocol used, both $TC_{untreated}$ and $TC_{extracted}$ were determined as the
122 averages of total carbon results from IMPROVE-A and NIOSH. A benefit of this approach was that
123 the uncertainty of MSOC (σ) could be estimated for each sample based on the parallel TC
124 measurements by different protocols:

125 $$\sigma = \sqrt{\left(\text{SD of } TC_{untreated}\right)^2 + \left(\text{SD of } TC_{extracted}\right)^2} \Big/ \left(TC_{untreated} - TC_{extracted}\right)$$

126 where SD indicates standard deviation. In this study, σ averaged $3.3 \pm 2.9\%$ with a median of 2.4%.

In addition, organic compounds that are in-soluble in methanol, i.e., MIOC, was measured as the organic carbon concentration of the extracted punch. Unless stated otherwise, (i) OC involved in the following discussions indicates the sum of MSOC and MIOC, and correspondingly, EC indicates elemental carbon measured by the extracted punch; and (ii) all the carbonaceous aerosol concentrations are based on IMPROVE-A, except MSOC which did not rely on analytical protocol. The MSOC to OC ratios averaged 0.90 ± 0.05, indicating an overall high extraction efficiency of methanol for dissolving organic aerosols.

Light absorption spectra of the methanol extracts were measured over the wavelength (λ) range of 200–1110 nm, using a spectrophotometer coupled with a 2.5-m long liquid waveguide capillary cell (LWCC; World Precision Instrument, FL, USA). The spectrophotometer, consisting of a DH-mini UV-VIS-NIR light source and a Maya2000 Pro spectrometer (Ocean Optics Inc., FL, USA), provided wavelength-resolved optical attenuation (ATN_λ) of the dissolved BrC, which could then be converted to BrC absorption coefficient [$(b_{abs})_\lambda$] (Hecobian et al., 2010). The ratio of $(b_{abs})_\lambda$ to MSOC concentration was considered the bulk mass absorption efficiency (MAE_λ) of brown carbon, given the close-to-one MSOC/OC. The wavelength dependence of BrC absorption was determined based on $\ln(ATN_\lambda)$ and $\ln(\lambda)$, and was expressed as the absorption Ångström exponent (AAE). The AAE calculation was performed over 310–460 nm, the same λ range adopted by previous studies conducted at the same site using the same laboratory analysis procedures (Cheng et al., 2022a).

2.3 Additional data sets used

Air quality data and meteorological data were obtained with a time resolution of 1 hour from the China National Environmental Monitoring Center (CNEMC; https://air.cnemc.cn:18007/, last access: 1 January, 2023) and Weather Underground (https://www.wunderground.com/, last access:

1 January, 2023), respectively. CNEMC operated 12 monitoring sites in Harbin, with 3 of them located within ~5 km from the HIT sampling site. The reconstructed $PM_{2.5}$ masses, which were derived from observational results on aerosol compositions at HIT, were generally in line with the fine particle concentrations directly measured at the nearby CNEMC sites. Here the reconstructed $PM_{2.5}$ was calculated as the sum of organic matter (1.6 × OC), elemental carbon and inorganic ions. Comparison of the reconstructed and directly-measured $PM_{2.5}$ concentrations showed relative standard deviations of 9–11% (in terms of median value) for the three CNEMC sites nearby, demonstrating HIT as a representative urban site for Harbin. In this study, only the air quality data from the nearest CNEMC site, i.e., Taiping Hongwei Park, were further investigated together with the aerosol components measured at HIT.

3. Results and discussion

3.1 Why was the wintertime brown carbon more absorbing at night?

The wavelength-resolved b_{abs} and MAE were primarily explored at 365 nm, and the corresponding values were referred to as $(b_{abs})_{365}$ and MAE_{365}, respectively. $(b_{abs})_{365}$ and MSOC correlated strongly for the winter campaign (Figure 1a), that the linear regression of $(b_{abs})_{365}$ against MSOC led to an r value of 0.97 and a slope of 1.63 ± 0.02 m^2/gC (with the intercept set as zero; MAE_{365} averaged 1.55 ± 0.18 m^2/gC). However, as shown in Figure 1b, the nighttime samples were found to exhibit higher MAE_{365} values (averaging 1.61 ± 0.15 m^2/gC) than the daytime ones (averaging 1.48 ± 0.18 m^2/gC), with significant differences at the 95% confidence level (2-tailed p = 0.004). In this study, we did not perform source apportionment analysis for brown carbon due to the relatively small number of samples collected. Instead, several indirect indicators were introduced to interpret the diurnal variations of MAE_{365}. Statistical results for the comparisons

performed in the following discussions are summarized in Table S1.

The first indicator was the levoglucosan to OC ratio (LG/OC; on a basis of carbon mass, the same hereinafter). In general, higher LG/OC values indicate a stronger contribution of biomass burning (BB) emissions to OC. The BB activities in January could be attributed primarily to household use of biofuels, e.g., for heating and cooking. This is because (i) few fire hotspot was detected in Harbin and surrounding regions throughout the winter campaign (Figure 2a), and (ii) the relationship between LG and water-soluble potassium (K^+), another commonly-used BB tracer, did not show evidence for apparent influence of open burning (Figure 3a). As suggested by previous studies conducted during heating season in Harbin (Cheng et al., 2022b), the LG to K^+ ratios were relatively low and constant (~0.5) with the absence of agricultural fires, but became substantially higher (typically above 1.0) during open burning episodes. This pattern was attributed to the relatively low combustion efficiencies (CE) of agricultural fires, which favored the increase of LG emissions but would not change K^+ emissions significantly (Gao et al., 2003). It should be noted that in Cheng et al. (2022b), CE were not directly measured for different types of burning activities and instead were investigated based on the ratios of BB organic carbon to BB elemental carbon (R_{BB}, derived from positive matrix factorization, i.e., PMF, analysis). Substantial increases of R_{BB} were repeatedly observed during open burning episodes occurring in different seasons, e.g., winter or spring depending on the regulatory policies. Thus the agricultural fires were inferred to have relatively low CE levels compared to residential burning of crop residues (Cheng et al., 2022b), as BB source emission studies typically showed a decreasing trend for the emission ratio of organic carbon to elemental carbon with increasing combustion efficiency (Pokhrel et al., 2016; McClure et al., 2020). Actually, crop residues burned on farmland were usually not intentionally dried and thus

could have relatively high water contents. This may partially explain the relatively low CE of agricultural fires. In the present study, LG correlated strongly with K^+ for the entire January (r = 0.96, with a slope, i.e., $\Delta LG/\Delta K^+$, of 0.55 ± 0.02; Figure 3a) and the LG to K^+ ratios averaged 0.46 ± 0.11, pointing to the dominance of residential burning in BB emissions. In addition, the residential burning activities were more intensive at night, as can be seen from the elevated LG/OC compared to daytime results (1.10 ± 0.26% vs. 0.88 ± 0.22%, 2-tailed p = 0.001; Figure 1c). Comparison of the LG to EC ratios between the nighttime and daytime samples (0.22 ± 0.06 vs. 0.15 ± 0.05, 2-tailed p = 0.000) reached the same conclusion. Indeed, biomass burning could emit a number of strong chromophores such as nitrogen-containing aromatic compounds (Mohr et al., 2013; Lin et al., 2016, 2017; Xie et al., 2019; Salvador et al., 2021). However, for the January samples, MAE_{365} did not show clear dependence on LG/OC or LG/EC (r = 0.42 and 0.12, respectively; Figure 1e), suggesting that in addition to BB emissions, there must exist other factors that were more responsible for the diurnal variations of wintertime MAE_{365}.

The second indicator was $R_{S/N}$, defined as the ratio of (n-sulfur dioxide + n-sulfate) to (n-nitrogen dioxide + n-nitrate), where "n" indicates molar concentration. Given that sulfate and nitrate are typically considered as secondary, $R_{S/N}$ could be roughly traced back to the emission ratios of sulfur dioxide (SO_2) to nitrogen oxides (NO_x), i.e., $E_{S/N}$, from combustion of various types of fuels (e.g., coal, gasoline, diesel and biomass). Previous studies suggested that $E_{S/N}$ differed substantially between emissions from vehicles, coal combustion and biomass burning. In China, the fuel quality standards have been greatly strengthened for on-road vehicles since early 2000s, e.g., the maximum sulfur content allowed in diesel was reduced from 2000 ppm (required by the China I standard implemented in 2002) to 10 ppm (required by the China V standard implemented in 2017). Thus,

recent studies on vehicular exhausts typically suggested that the SO_2 emission factors (EF-SO_2) were about two orders of magnitude lower than those of NOx (EF-NOx; Zhang et al., 2015; Li et al., 2019) and consequently, the corresponding $E_{S/N}$ should be approximately ~10^{-2}. EF-SO_2 were also usually lower than EF-NOx for biomass burning (Zhang et al., 2000; McMeeking et al., 2009; Liu et al., 2016; Wu et al., 2022), but their differences were not as large as those observed in vehicle emissions, leading to $E_{S/N}$ values of ~10^{-1}. Unlike vehicles or biomass burning, coal combustion usually resulted in higher EF-SO_2 compared to EF-NOx (Zhang et al., 2000; Du et al., 2017; Li et al., 2017), which could be translated to $E_{S/N}$ values of above one. On the other hand, primary species could be transformed rapidly during atmospheric aging, e.g., a sharp loss of NO_x and a corresponding burst in nitrate were observed shortly after emission when tracking plumes from diesel trucks (Shen et al., 2021) and agricultural fires (Akagi et al., 2012; Liu et al., 2016). Thus it should be acceptable to assume that for the pollutants emitted by a specific source, the $R_{S/N}$ of aged plumes was generally comparable with the $E_{S/N}$ of fresh emissions.

The ambient $R_{S/N}$ averaged 0.6 ± 0.2 during the winter campaign, differing substantially from the $E_{S/N}$ of coal combustion or vehicle emissions but in the same order of magnitude as the $E_{S/N}$ of biomass burning. Actually, no evidence supported BB emissions as a major regulating factor for $R_{S/N}$, e.g., as indicated by the insignificant correlations between $R_{S/N}$ and LG/EC (r = 0.24 and 0.01 for the daytime and nighttime samples, respectively). Then $R_{S/N}$ was expected to be more sensitive to the changes of coal combustion and vehicle emissions, e.g., increase of coal combustion emissions would effectively elevate $R_{S/N}$ whereas higher vehicle emissions favor the decrease of $R_{S/N}$. During the winter campaign, lower $R_{S/N}$ were observed at night (Figure 1d), averaging 0.5 ± 0.1 compared to an average $R_{S/N}$ of 0.7 ± 0.2 for the daytime samples (2-tailed p = 0.000). In

principle, this pattern could be caused by decreased coal combustion emissions and/or increased vehicle emissions at night. However, it seemed that the former did not play an important role, since many coal combustion activities (e.g., those for heating supply, power generation and some industrial processes) were uninterruptible, i.e., would not be stopped at night (Lian et al., 2020; Chu et al., 2021; Yuan et al., 2021). Then the most likely cause for the lower nighttime $R_{S/N}$ was increased vehicle emissions. According to the Road Traffic Regulations released by Harbin, heavy-duty diesel trucks (HDDT), which are known to include high- or super-emitters (Dallmann et al., 2012), are allowed to run on the roads in the main urban area only from 21:00 to 5:00 of the next day. This to a large extent explains the inference on the increase of vehicle emissions during nighttime. MAE_{365} exhibited a clear negative dependence on $R_{S/N}$ for all the winter samples (Figure 1f), suggesting vehicle emissions, especially those from HDDT, as a dominant influencing factor for MAE_{365} (under the precondition of relatively stable coal combustion emissions).

The last two indicators were associated with secondary aerosol formation, including the sulfur oxidation ratio (SOR) and the nitrogen oxidation ratio (NOR) defined as n-sulfate/(n-sulfate + n-SO_2) and n-nitrate/(n-nitrate + n-NO_2), respectively. The entire winter campaign experienced low temperatures, which averaged –16 ± 5 and –21 ± 6 °C for the daytime and nighttime samples, respectively. In general, the transformation of gaseous precursors to secondary inorganic ions was inefficient in the frigid atmosphere, as indicated by the overall low levels of both SOR and NOR. However, both indicators exhibited noticeable differences between daytime and nighttime samples. The diurnal variation of SOR was found to be associated with the higher relative humidity (RH) levels at night (Figure 4a). For the vast majority of winter samples, RH fell into the ranges of 60–80 and 70–90% during daytime and nighttime, respectively. SOR were largely unchanged when RH

increased from 60–70% to 70–80% during the day, whereas for the common RH range shared by the daytime and nighttime samples (i.e., 70–80%), SOR tended to be slightly lower at night, likely due to the drop of temperatures. In addition, a positive dependence of SOR on RH was evident for the nighttime samples. Although SOR showed almost the same median values (~0.1) for the RH ranges of 70–80 and 80–90% at night, relatively high SOR levels of above 0.2 were more frequently observed in the latter case. Such high SOR were rarely seen during the day, indicating that RH played a more important role than temperature in sulfate formation. The enhanced sulfate formation at high RH was presumably through heterogeneous reactions (Su et al., 2020; Liu et al., 2021), since the low temperatures encountered during the winter campaign did not rule out the presence of aerosol water, e.g., liquid water was observed to remain super-cooled in clouds down to temperatures of as low as –40 °C (Tabazadeh et al., 2002). Compared to SOR, different patterns of diurnal variation were observed for NOR (Figure 4b). First, the difference between daytime and nighttime NOR was more significant for the RH range of 70–80%, e.g., as indicated by the larger decrease of median NOR at night (0.06, compared to a corresponding value of 0.02 for SOR). Second, the nighttime NOR elevated substantially as RH increased from 70–80% to 80–90%, but still with lower levels compared to the daytime results. Given that relatively low temperatures favor the partitioning of semi-volatile nitrate into aerosol phase, the less efficient nitrate formation at night could not be explained by the partitioning process and instead should be primarily attributed to reduced photooxidation of NO_2 (Chen et al., 2020). Based on a synthesis of the diurnal variations observed for SOR and NOR, the nighttime samples were characterized by enhanced heterogeneous chemistry, which did not require sunlight as indicated by the RH-dependent increase of SOR under dark conditions, and weakened photochemical reactions. The overall effect of these two factors on

281 secondary organic aerosol (SOA) formation was inconclusive and thus it remained difficult to
282 robustly unfold the role of SOA in the diurnal variations of MAE_{365}. Actually, it appeared that
283 MAE_{365} was not strongly influenced by SOA during the winter campaign. For example, when RH
284 increased from 70–80% to 80–90% at night, the MAE_{365} were nearly constant (e.g., with the same
285 average value of 1.6 m^2/gC for the two RH ranges) despite the enhancement of heterogeneous
286 chemistry.

287 **3.2 Why did the springtime MAE_{365} show more significant diurnal variations?**

288 Compared to the wintertime results, the average MAE_{365} was lower in spring (1.33 vs. 1.55
289 m^2/gC) but the corresponding standard deviation was much higher (0.62 vs. 0.18 m^2/gC), indicating
290 that the spring samples varied more significantly with respect to the absorption capacity of brown
291 carbon (Figure 5a). This feature could also be seen from the more pronounced diurnal variations of
292 MAE_{365} observed in spring (Figure 5b), e.g., the nighttime MAE_{365} were on average ~70% (2-tailed
293 $p = 0.000$) and 10% (2-tailed $p = 0.004$) larger than the daytime values during the spring and winter
294 measurement periods, respectively. For the winter campaign, the slightly elevated MAE_{365} at night
295 had been primarily attributed to increased vehicle emissions, as indicated by a ~35% decrease of
296 $R_{S/N}$. In spring, $R_{S/N}$ were also lower at night (2-tailed $p = 0.000$), by ~40% compared to the daytime
297 results (Figure 5d). Given that the two campaigns showed comparable discrepancies between the
298 nighttime and daytime $R_{S/N}$, increase of vehicle emissions at night was presumably not the dominant
299 driver for the much stronger diurnal variations of MAE_{365} observed in spring. Actually, MAE_{365} was
300 almost independent of $R_{S/N}$ for the spring samples. For example, the MAE_{365} values were found to
301 fall into two well-separated ranges (above 2 and ~0.5–1.5 m^2/gC, with the former observed only at
302 night) for the samples with relatively low $R_{S/N}$ levels (below 0.4), indicating that reduced $R_{S/N}$ was

303 ineffective to explain the high MAE_{365} events encountered in spring (Figure 5f). In addition to
304 increased vehicle emissions at night, therefore, there must exist other factors which were more
305 responsible for the significant diurnal variations of springtime MAE_{365}.

306 We first evaluated the influence of secondary aerosol formation. The spring campaign
307 experienced lower RH and substantially higher temperatures compared to winter, by ~25% and
308 30 ℃, respectively. The springtime SOR appeared to be slightly lower than the wintertime results
309 (0.12 ± 0.06 vs. 0.15 ± 0.07), whereas an opposite pattern was observed for NOR (0.16 ± 0.08 vs.
310 0.12 ± 0.06). The seasonal variations of SOR and NOR provided additional evidence for the
311 inferences that the sulfate and nitrate formation was more strongly contributed by heterogeneous
312 and photochemical reactions, respectively. For the spring campaign, the daytime and nighttime SOR
313 were in general comparable (Figure S1a) and no clear evidence was observed for the prevalence of
314 heterogeneous chemistry, presumably due to the rare occurrence of high RH conditions either during
315 the day or at night. Unlike SOR, the daytime NOR tended to be slightly higher than the nighttime
316 results (0.18 ± 0.09 vs. 0.14 ± 0.08; Figure S1b), pointing to enhanced photochemistry during the
317 day. This pattern could be partially responsible for the relatively low daytime MAE_{365}, since
318 secondary brown carbon was typically less light-absorbing than primary BrC (Kumar et al., 2018;
319 Cappa et al., 2020; Ni et al., 2021). However, MAE_{365} did not exhibit clear dependence on NOR or
320 the nitrate to OC ratio (NO_3^-/OC), e.g., the high MAE_{365} events were found to be associated with
321 moderate NOR and NO_3^-/OC levels (Figure S2). Thus for the spring campaign, photochemistry
322 should not be the major influencing factor for MAE_{365}, either.

323 We then investigated the role of biomass burning. Unlike the wintertime results, MAE_{365}
324 showed a strong positive correlation with LG/OC (r = 0.84) in spring (Figure 5e), suggesting

biomass burning emissions as the dominant driver for the variations of MAE_{365}. It is noteworthy that the LG to OC ratios were substantially higher in spring than in winter (2-tailed $p = 0.000$), with averages of 3.11 ± 1.70% and 0.99 ± 0.26%, respectively. This pattern could not be explained by seasonal variations in residential consumption of biofuels, since April experienced much higher temperatures than January (averaging 11 and –19 °C, respectively). Instead, the elevated springtime LG/OC should be attributed primarily to open burning, as supported by the intensive fire hotspots detected around Harbin in April (Figure 2b). The seasonal variations of LG to K^+ ratio (LG/K^+) also suggested that the dominant burning ways were different between winter and spring. Compared to the relatively small and constant LG/K^+ observed in January (0.46 ± 0.11), the ratios were nearly tripled in April (1.28 ± 0.61) with more significant sample-by-sample differences (between ~0.5–3.5) (Figure 3b). Recalling that the transition from flaming to smoldering combustion favored the increase of LG/K^+ (Gao et al., 2003), the springtime burning should have relatively low and variable combustion efficiencies. This inference was in line with the fact that the agricultural fires were usually uncontrolled, e.g., with respect to water content of crop residues and abundance of oxygen. In all, for the spring campaign, the dominant driver for the variations of LG/OC and MAE_{365} could be further identified as open burning. Subsequently, the higher LG/OC and MAE_{365} at night (Figures 5b–5c) could be attributed primarily to increased agricultural fires. The preference on nighttime burning was not surprising, since the agricultural fires were illegal, i.e., nominally prohibited by the Government of Heilongjiang Province.

It should be noted that the agricultural fire emissions increased LG/OC but had minimal influence on $R_{S/N}$ (Figure S3). For example, the nighttime samples collected in spring differed substantially with respect to the impact of agricultural fires, as indicated by their variable LG/OC

which spanned nearly one order of magnitude. However, no clear pattern was observed for $R_{S/N}$ with increasing LG/OC, e.g., linear regression of $R_{S/N}$ on LG/OC showed an extremely low r value of 0.07.

The frequent occurrences of agricultural fires during April, 2021 to some extent masked the "background" MAE_{365}, i.e., the value representative for the spring conditions without significant influence of open burning. In spring, all the samples with LG/K^+ ratios of above one, i.e., a chemical signature for apparent impacts of agricultural fires, were found to have LG/OC ratios larger than 2%. In addition, LG/OC ratio could also work as an estimate of the strength of biomass burning impact. Thus in the following discussions, LG/OC of > 2% was used as an indicator for open burning episodes and correspondingly, spring samples with LG/OC of below 2% were referred to as typical ones. MAE_{365} averaged 0.80 ± 0.22 m^2/gC for the typical samples of spring, lower than results from the winter campaign (1.55 ± 0.18 m^2/gC; Figure S4a). This seasonal pattern coincided with the overall lower $R_{S/N}$ in spring (Figure S4b). It was unlikely that the number of in-use vehicles or the fleet composition in Harbin could vary significantly between January and April of the same year. Thus the reduced springtime $R_{S/N}$, i.e., the relatively low MAE_{365} with the absence of agricultural fires, should be caused mainly by the decrease of coal combustion emissions, e.g., due to the less demand for heating.

3.3 Unique wavelength dependence of BrC absorption during agricultural fire episodes

The agricultural fires not only elevated MAE_{365} but also changed the wavelength dependence of brown carbon. For the wavelength range used for AAE calculation (310–460 nm), the detection limit of optical attenuation (ATN_{LOD}) was ~0.02, which was determined as three times the maximum standard deviation of parallel ATN_λ results from blank filters. Before further discussions, we

introduced a new term "relative $\ln(ATN_\lambda)$", i.e., $\ln(ATN_\lambda)^*$ calculated as $\ln(ATN_\lambda) - \ln(ATN_{LOD})$. A benefit of using the new term was that a $\ln(ATN_\lambda)^*$ value of zero corresponded to $ATN_\lambda = ATN_{LOD}$ and thus $\ln(ATN_\lambda)^*$ could be considered "real" absorption by chromophores in solutions. It should be noted that the use of $\ln(ATN_\lambda)^*$ would not influence the determination of AAE, since the same slope would be derived from the regressions of $\ln(ATN_\lambda)^*$ and $\ln(ATN_\lambda)$ on $\ln(\lambda)$. For the typical samples of spring, the dependence of $\ln(ATN_\lambda)^*$ on $\ln(\lambda)$ could be properly approximated by a linear function, usually with r values of above 0.995. In this case, AAE could be reliably determined, and an average value of 6.92 ± 0.28 was obtained.

The relationship between $\ln(ATN_\lambda)^*$ and $\ln(\lambda)$ became non-linear for the open burning episodes. To more quantitatively describe the non-linearity, we added an "auxiliary line" to each measured spectrum (Figure 6a), by drawing a line between the two points with x values of ln(310) and ln(460). The "auxiliary line" could be considered an assumed spectrum with linear dependence of $\ln(ATN_\lambda)^*$ on $\ln(\lambda)$. The measured spectrum was always above the assumed one and their largest difference was typically observed at ~365 nm, pointing to the presence of distinct BrC chromophores with absorption peak around this wavelength.

The influence of such chromophores on BrC absorption could be estimated by the following three indicators. The first one (F) was related to the difference between the measured and assumed $\ln(ATN_\lambda)^*$ at 365 nm: $F = \left[\ln\left(ATN_{365}\right)^*_m - \ln\left(ATN_{365}\right)^*_a\right] \Big/ \ln\left(ATN_{365}\right)^*_a$, where the subscripts "m" and "a" indicate results from the measured and assumed spectra, respectively (Figure 6a). The second indicator (K) was related to the area enclosed between the two spectra (S_2): $K = S_2/S_1$, where S_1 indicates the area enclosed by the assumed spectrum and x-axis (Figure 6b). The last indicator was $\Delta(b_{abs})_{365}$

calculated as $(b_{abs})^{m}_{365} - (b_{abs})^{a}_{365}$, where the superscripts "m" and "a" indicate absorption coefficients calculated based on the measured and assumed spectra, respectively. *F* and *K* exhibited a strong linear correlation for the open burning episodes (r = 0.99; Figure 6c), indicating that the differences between the measured and assumed spectra were likely caused by the same class of BrC compounds. In addition, these compounds could be primarily traced back to biomass burning, since $\Delta(b_{abs})_{365}$ showed a positive dependence on LG/OC (Figure 6d). Candidates for such compounds were aromatic species with nitro-functional groups, based on a synthesis of absorption spectra measured for various BrC chromophores (Huang et al., 2020) and molecular characterization results for biomass burning emissions (Lin et al., 2016, 2017; Xie et al., 2019, 2020). Chamber experiments by Iinuma et al. (2010) suggested that aromatic compounds with nitro-functional groups could also be formed through photooxidation of gaseous precursors emitted by biomass burning (*m*-cresol). In this study, however, all the samples with relatively high $\Delta(b_{abs})_{365}$ levels (e.g., above 20 Mm^{-1}) were collected at night, indicating that the distinct BrC chromophores with absorption peak at ~365 nm were more strongly associated with primary emissions from agricultural fires. In addition, the chromophores seemed to be subject to photo-bleaching, as both *F* and *K* decreased substantially (by ~65%) during the day compared to the nighttime results (Figure 7).

For the open burning episodes, the distinct absorption peak at ~365 nm prohibited a proper determination of AAE. If enforcing a linear function for the dependence of $\ln(ATN_\lambda)^*$ on $\ln(\lambda)$, lower r values would be derived (down to ~0.97, with an average of 0.992 ± 0.007) compared to the typical samples (averaging 0.998 ± 0.002). In addition, r showed decreasing trends with the increases of LG/OC (Figure 6e) and *F* (Figure S5), suggesting that the relationship between $\ln(ATN_\lambda)^*$ and $\ln(\lambda)$ deviated more significantly from linearity as the ~365 nm absorption peak, i.e., the influence of

agricultural fires, became more significant. We suggest that for the open burning episodes, the AAE results should be interpreted with caution, although they could be calculated mathematically with reasonable *r* values (e.g., even the minimum *r* appeared acceptable).

3.4 Diurnal variations of wintertime AAE

Similar to the typical samples of spring, $\ln(ATN_\lambda)^*$ exhibited linear dependences on $\ln(\lambda)$ for all the winter samples. The wintertime AAE were higher at night compared to those observed during the day (with averages of 7.33 ± 0.14 and 6.76 ± 0.11, respectively; 2-tailed $p = 0.000$), consistent with the pattern observed during winter in Beijing (Li et al., 2020). The relative abundance of secondary OC (SOC) has been considered an important influencing factor for AAE, e.g., an increasing trend was observed for AAE during long-range transport of BrC over the Indo-Gangetic Plain (Dasari et al., 2019). Although SOC or its organic tracer was not determined in this study, previous source apportionment results from Harbin (based on PMF) showed a strong correlation between SOC and sulfate, with largely consistent relationships among different campaigns (Cheng et al., 2022b). Thus we used sulfate as an indicator for SOC. During the winter campaign, the sulfate to OC ratios were lower at night (averaging 0.38, compared to 0.44 during the day; 2-tailed $p = 0.011$), pointing to decreased fractions of SOC in OC. This inference was consistent with the higher LG/OC and $R_{S/N}$ levels observed at night, which had been attributed to increased emissions from residential biomass burning and vehicular exhausts, respectively. Thus regarding the association between AAE and SOC formation, results from the winter campaign were inconsistent with Dasari et al. (2019), but the reason remained unclear. Molecular characterization of organic aerosols should be necessary to unfold the response of AAE to changes in BrC sources.

4. Conclusions and atmospheric implications

435 Diurnal variations of BrC were investigated during two distinct seasons in the northernmost
436 megacity in China. The winter campaign was characterized by low temperatures rarely seen in other
437 hotspots of air pollution studies such as the North China Plain. The wintertime BrC aerosols were
438 slightly more absorbing at night, with an average MAE_{365} of 1.61 ± 0.15 m^2/gC compared to 1.48 ±
439 0.18 m^2/gC during the day. Various indicators were used to explain the observed diurnal variations
440 of MAE_{365}, including those associated with biomass burning emissions (LG/K^+ and LG/OC),
441 relative importance of coal combustion and vehicle emissions ($R_{S/N}$) and secondary aerosol
442 formation (SOR and NOR). For the winter campaign, the nighttime samples were characterized by
443 increased BB emissions from residential sources, enhanced heterogeneous chemistry and weakened
444 photochemical reactions. But none of these factors was identified as the dominant driver for the
445 higher MAE_{365} at night. Instead, MAE_{365} exhibited a negative dependence on $R_{S/N}$, and the lower
446 $R_{S/N}$ and thus higher MAE_{365} at night were primarily attributed to increased emissions from heavy-
447 duty diesel trucks, which were not allowed in the main urban area during the day. In addition, the
448 wintertime AAE were higher at night but it remained difficult to unfold the underlying connection
449 between this diurnal pattern and the changes in BrC sources.

450 The spring campaign was characterized by frequent occurrences of agricultural fires, with more
451 pronounced diurnal variations of MAE_{365} (averaging 0.98 ± 0.31 and 1.69 ± 0.65 m^2/gC for the
452 daytime and nighttime samples, respectively). Unlike winter, the springtime MAE_{365} were mainly
453 influenced by open burning emissions, as suggested by the positive dependence of MAE_{365} on
454 LG/OC and the lack of correlation between MAE_{365} and $R_{S/N}$. The higher nighttime LG/OC
455 indicated that the farmers preferred burning the crop residues at night, presumably because
456 agricultural fires were nominally prohibited by the local government. In addition, BrC exhibited

457 distinct light absorption spectra during agricultural fire episodes, as indicated by the non-linear
458 relationship between $\ln(ATN_\lambda)^*$ on $\ln(\lambda)$. The non-linearity was mainly caused by chromophores
459 with absorption peak at ~365 nm, which became more significant with increasing BB influence.
460 Aromatic species with nitro-functional groups were a possible class of compounds that were at play.
461 The presence of such chromophores, i.e., the distinct absorption peak at ~365 nm, prohibited a
462 proper determination of AAE for the spring samples impacted by agricultural fires.

463 MAE_{365} and AAE are key parameters for simulating climate effects of brown carbon. In winter,
464 although Harbin experiences low temperatures rarely seen in other Chinese megacities, the observed
465 MAE_{365} and AAE were largely comparable with the typical results from other regions in Northern
466 China (e.g., Beijing; Cheng et al., 2016). In addition, BrC's optical properties were indeed different
467 between daytime and nighttime samples, which were likely associated with increased HDDT
468 emissions at night. However, the diurnal variations (~10% higher at night for both MAE_{365} and AAE)
469 appeared negligible compared to uncertainties in simulating the mass concentration of BrC, i.e.,
470 organic aerosol. Thus for typical winter conditions in Northern China (without open burning), it
471 may be practical to use fixed MAE_{365} and AAE values for estimating the wavelength-resolved
472 absorption by organic aerosol in climate models.

473 The spring campaign suggested another scenario, that the agricultural fires exhibited strong
474 influences on optical properties of brown carbon, as highlighted by the ~365 nm peak in BrC's
475 absorption spectra. The distinct peak on one hand effectively elevated MAE_{365}, and on the other
476 hand complicated the determination of AAE. In addition, the peak became less significant during
477 the day, indicating that the organic compounds at play were likely subject to photo-bleaching. BrC
478 emitted by the fires remained difficult to constrain, partially due to the variable combustion

efficiencies. This in turn resulted in challenges for simulating climate effects of the open burning aerosols. Given the massive agricultural sector in Northeast China, more studies are necessary to understand the emissions, transformation and impacts of the fire-induced pollutants.

Data availability. Data described in this manuscript can be accessed at https://doi.org/10.5281/zenodo.7874760 (Cheng, 2023).

Author contributions. YC and JL designed the study and prepared the paper with inputs from all the co-authors. XC, YZ and QY carried out the experiments. QZ and KH validated the results and supervised the study.

Competing interests. Author Qiang Zhang is a member of the editorial board of *Atmospheric Chemistry and Physics*. The peer-review process was guided by an independent editor, and the authors have also no other competing interests to declare.

Acknowledgements. The authors thank Zhen-yu Du at National Research Center for Environmental Analysis and Measurement, and Lin-lin Liang at Chinese Academy of Meteorological Sciences for their help in sample analysis.

Financial support. This research has been supported by the National Natural Science Foundation of China (42222706), the Natural Science Foundation of Heilongjiang Province (LH2020D011), Fundamental Research Funds for the Central Universities, and Heilongjiang Touyan Team.

References

Akagi, S. K., Craven, J. S., Taylor, J. W., McMeeking, G. R., Yokelson, R. J., Burling, I. R., Urbanski, S. P., Wold, C. E., Seinfeld, J. H., Coe, H., Alvarado, M. J., and Weise, D. R.: Evolution of trace gases and particles emitted by a chaparral fire in California, ***Atmos. Chem. Phys.***, 12, 1397–1421, https://doi.org/10.5194/acp-12-1397-2012, 2012.

Brege, M. A., China, S., Schum, S., Zelenyuk, A., and Mazzoleni, L. R.: Extreme molecular complexity resulting in a continuum of carbonaceous species in biomass burning tar balls from wildfire smoke, ***ACS Earth Space Chem.***, 5, 2729–2739,

https://doi.org/10.1021/acsearthspacechem.1c00141, 2015.

Brown, H., Liu, X. H., Feng, Y., Jiang, Y. Q., Wu, M. X., Lu, Z., Wu, C. L., Murphy, S., and Pokhrel, R.: Radiative effect and climate impacts of brown carbon with the Community Atmosphere Model (CAM5), ***Atmos. Chem. Phys.***, 18, 17745–17768, https://doi.org/10.5194/acp-18-17745-2018, 2018.

Cappa, C. D., Lim, C. Y., Hagan, D. H., Coggon, M., Koss, A., Sekimoto, K., de Gouw, J., Onasch, T. B., Warneke, C., and Kroll, J. H.: Biomass-burning-derived particles from a wide variety of fuels – Part 2: effects of photochemical aging on particle optical and chemical properties, ***Atmos. Chem. Phys.***, 20, 8511–8532, https://doi.org/10.5194/acp-20-8511-2020, 2020.

Chen, X. R., Wang, H. C., Lu, K. D., Li, C. M., Zhai, T. Y., Tan, Z. F., Ma, X. F., Yang, X. P., Liu, Y. H., Chen, S. Y., Dong, H. B., Li, X., Wu, Z. J., Hu, M., Zeng, L. M., and Zhang, Y. H.: Field determination of nitrate formation pathway in winter Beijing, ***Environ. Sci. Technol.***, 54, 9243–9253, https://doi.org/10.1021/acs.est.0c00972, 2020.

Chen, Y., and Bond, T. C.: Light absorption by organic carbon from wood combustion, ***Atmos. Chem. Phys.***, 10, 1773–1787, https://doi.org/10.5194/acp-10-1773-2010, 2010.

Cheng, Y.: Diurnal variations of brown carbon during two distinct seasons in a megacity in Northeast China [data set], https://doi.org/10.5281/zenodo.7874760, 2023.

Cheng, Y., He, K. B., Du, Z. Y., Engling, G., Liu, J. M., Ma, Y. L., Zheng, M., and Weber, R. J.: The characteristics of brown carbon aerosol during winter in Beijing, ***Atmos. Environ.***, 127, 355–364, https://doi.org/10.1016/j.atmosenv.2015.12.035, 2016.

Cheng, Y., Cao, X. B., Liu, J. M., Yu, Q. Q., Wang, P., Yan, C. Q., Du, Z. Y., Liang, L. L., Zhang, Q., and He, K. B.: Primary nature of brown carbon absorption in a frigid atmosphere with strong haze chemistry, ***Environ. Res.***, 204, 112324, https://doi.org/10.1016/j.envres.2021.112324, 2022a.

Cheng, Y., Cao, X. B., Liu, J. M., Yu, Q. Q., Zhong, Y. J., Geng, G. N., Zhang, Q., and He, K. B.: New open burning policy reshaped the aerosol characteristics of agricultural fire episodes in Northeast China, ***Sci. Total Environ.***, 810, 152272, https://doi.org/10.1016/j.scitotenv.2021.152272, 2022b.

Chu, B. W., Zhang, S. P., Liu, J., Ma, Q. X., and He, H.: Significant concurrent decrease in $PM_{2.5}$ and NO_2 concentrations in China during COVID-19 epidemic, ***J. Environ. Sci.***, 99, 346–353, https://doi.org/10.1016/j.jes.2020.06.031, 2021.

Dallmann, T. R., DeMartini, S. J., Kirchstetter, T. W., Herndon, S. C., Onasch, T. B., Wood, E. C., and Harley, R. A.: On-road measurement of gas and particle phase pollutant emission factors

for individual heavy-duty diesel trucks, ***Environ. Sci. Technol.***, 46, 8511–8518, https://doi.org/10.1021/es301936c, 2012.

Dasari, S., Andersson, A., Bikkina, S., Holmstrand, H., Budhavant, K., Satheesh, S., Asmi, E., Kesti, J., Backman, J., Salam, A., Bisht, D. S., Tiwari, S., Hameed, Z., and Gustafsson, Ö.: Photochemical degradation affects the light absorption of water-soluble brown carbon in the South Asian outflow, ***Sci. Adv.***, 5, eaau8066, https://doi.org/10.1126/sciadv.aau8066, 2019.

Du, W., Shen, G. F., Chen, Y. C., Zhu, X., Zhuo, S. J., Zhong, Q. R., Qi, M., Xue, C. Y., Liu, G. Q., Zeng, E., Xing, B. S., and Tao, S.: Comparison of air pollutant emissions and household air quality in rural homes using improved wood and coal stoves, ***Atmos. Environ.***, 166, 215–223, https://doi.org/10.1016/j.atmosenv.2017.07.029, 2017.

Engling, G., Carrico, C. M., Kreidenweis, S. M., Collett Jr., J. L., Day, D. E., Malm, W. C., Lincoln, L., Hao, W. M., Iinuma, Y., and Herrmann, H.: Determination of levoglucosan in biomass combustion aerosol by high-performance anion-exchange chromatography with pulsed amperometric detection, ***Atmos. Environ.***, 40, S299–S311, https://doi.org/10.1016/j.atmosenv.2005.12.069, 2006.

Gao, S., Hegg, D. A., Hobbs, P. V., Kirchstetter, T. W., Magi, B. I., and Sadilek, M.: Water-soluble organic components in aerosols associated with savanna fires in southern Africa: identification, evolution, and distribution, ***J. Geophys. Res.***, 108, D13, 8491, https://doi.org/10.1029/2002JD002324, 2003.

Hecobian, A., Zhang, X., Zheng, M., Frank, N., Edgerton, E. S., and Weber, R. J.: Water-soluble organic aerosol material and the light-absorption characteristics of aqueous extracts measured over the Southeastern United States, ***Atmos. Chem. Phys.***, 10, 5965–5977, https://doi.org/10.5194/acp-10-5965-2010, 2010.

Huang, R. J., Yang, L., Shen, J .C., Yuan, W., Gong, Y. Q., Guo, J., Cao, W. J., Duan, J., Ni, H. Y., Zhu, C. S., Dai, W. T., Li, Y. J., Chen, Y., Chen, Q., Wu, Y. F., Zhang, R. J., Dusek, U., and O'Dowd, C.: Water-Insoluble organics dominate brown carbon in wintertime urban aerosol of China: chemical characteristics and optical properties, ***Environ. Sci. Technol.***, 54, 7836–7847, https://doi.org/10.1021/acs.est.0c01149, 2020.

Huang, R. J., Yang, L., Shen, J. C., Yuan, W., Gong, Y. Q., Ni, H. Y., Duan, J., Yan, J., Huang, H. B., You, Q. H., and Li, Y. J.: Chromophoric fingerprinting of brown carbon from residential biomass burning, ***Environ. Sci. Technol. Lett.***, 9, 102–111, https://doi.org/10.1021/acs.estlett.1c00837, 2022.

Huo, Y. Q., Guo, Z. H., Li, Q., Wu, D., Ding, X., Liu, A. L., Huang, D., Qiu, G. K., Wu, M. M., Zhao, Z. J., Sun, H., Song, W. H., Li, X., Chen, Y. J., Wu, T. C., and Chen, J. M.: Chemical

fingerprinting of HULIS in particulate matters emitted from residential coal and biomass combustion, ***Environ. Sci. Technol.***, 55, 3593–3603, https://doi.org/10.1021/acs.est.0c08518, 2021.

Iinuma, Y., Böge, O., Gräfe, R., and Herrmann, H.: Methyl-nitrocatechols: atmospheric tracer compounds for biomass burning secondary organic aerosols, ***Environ. Sci. Technol.***, 44, 8453–8459, https://doi.org/10.1021/es102938a, 2010.

Jiang, H. X., Li, J., Sun, R., Tian, C. G., Tang, J., Jiang, B., Liao, Y. H., Chen, C. E., and Zhang, G.: Molecular dynamics and light absorption properties of atmospheric dissolved organic matter, ***Environ. Sci. Technol.***, 55, 10268–10279, https://doi.org/10.1021/acs.est.1c01770, 2021.

Kumar, N. K., Corbin, J. C., Bruns, E. A., Massabó, D., Slowik, J. G., Drinovec, L., Močnik, G., Prati, P., Vlachou, A., Baltensperger, U., Gysel, M., El-Haddad, I., and Prévôt, A. S. H.: Production of particulate brown carbon during atmospheric aging of residential wood-burning emissions, ***Atmos. Chem. Phys.***, 18, 17843–17861, https://doi.org/10.5194/acp-18-17843-2018, 2018.

Lack, D. A., Langridge, J. M., Bahreini, R., Cappa, C. D., Middlebrook, A. M., and Schwarz, J. P.: Brown carbon and internal mixing in biomass burning particles, ***Proc. Natl. Acad. Sci. USA***, 109, 14802–14807, https://doi.org/10.1073/pnas.1206575109, 2012.

Laskin, A., Laskin, J., and Nizkorodov, S. A.: Chemistry of atmospheric brown carbon, ***Chem. Rev.***, 115, 4335–4382, https://doi.org/10.1021/cr5006167, 2015.

Li, M., Liu, H., Geng, G. N., Hong, C. P., Liu, F., Song, Y., Tong, D., Zheng, B., Cui, H. Y., Man, H. Y., Zhang, Q., and He, K. B.: Anthropogenic emission inventories in China: a review, ***Natl. Sci. Rev.***, 4, 834–866, https://doi.org/10.1093/nsr/nwx150, 2017.

Li, X., Wang, Y. J., Hu, M., Tan, T. Y., Li, M. R., Wu, Z. J., Chen, S. Y., and Tang, X. Y.: Characterizing chemical composition and light absorption of nitroaromatic compounds in the winter of Beijing, ***Atmos. Environ.***, 237, 117712, https://doi.org/10.1016/j.atmosenv.2020.117712, 2019.

Li, Y. C., Liu, J., Han, H., Zhao, T. L., Zhang, X., Zhuang, B. L., Wang, T. J., Chen, H. M., Wu, Y., and Li, M. M.: Collective impacts of biomass burning and synoptic weather on surface $PM_{2.5}$ and CO in Northeast China, ***Atmos. Environ.***, 213, 64–80, https://doi.org/10.1016/j.atmosenv.2019.05.062, 2019.

Li, Y. R., Tan, Z. Q., Ye, C. X., Wang, J. X., Wang, Y. W., Zhu, Y., Liang, P. F., Chen, X., Fang, Y. H., Han, Y. Q., Wang, Q., He, D., Wang, Y., and Zhu, T.: Using wavelet transform to analyse on-road mobile measurements of air pollutants: a case study to evaluate vehicle emission

control policies during the 2014 APEC summit, ***Atmos. Chem. Phys.***, 19, 13841–13857, https://doi.org/10.5194/acp-19-13841-2019, 2019.

Lian, X. B., Huang, J. P., Huang, R. J., Liu, C. W., Wang, L. N., and Zhang, T. H.: Impact of city lockdown on the air quality of COVID-19-hit of Wuhan city, ***Sci. Total Environ.***, 742, 140556, https://doi.org/10.1016/j.scitotenv.2020.140556, 2020.

Lin, P., Aiona, P. K., Li, Y., Shiraiwa, M., Laskin, J., Nizkorodov, S. A., and Laskin, A.: Molecular characterization of brown carbon in biomass burning aerosol particles, ***Environ. Sci. Technol.***, 50, 11815–11824, https://doi.org/10.1021/acs.est.6b03024, 2016.

Lin, P., Bluvshtein, N., Rudich, Y., Nizkorodov, S. A., Laskin, J., and Laskin, A.: Molecular chemistry of atmospheric brown carbon inferred from a nationwide biomass burning event, ***Environ. Sci. Technol.***, 51, 11561–11570, https://doi.org/10.1021/acs.est.7b02276, 2017.

Lin, P., Fleming, L. T., Nizkorodov, S. A., Laskin, J., and Laskin, A.: Comprehensive molecular characterization of atmospheric brown carbon by high resolution mass spectrometry with electrospray and atmospheric pressure photoionization, ***Anal. Chem.***, 90, 12493–12502, https://doi.org/10.1021/acs.analchem.8b02177, 2018.

Lin, P., Laskin, J., Nizkorodov, S. A., and Laskin, A.: Revealing brown carbon chromophores produced in reactions of methylglyoxal with ammonium sulfate, ***Environ. Sci. Technol.***, 49, 14257–14266, https://doi.org/10.1021/acs.est.5b03608, 2015.

Liu, T. Y., Chan, A. W. H., and Abbatt, J. P. D.: Multiphase oxidation of sulfur dioxide in aerosol particles: implications for sulfate formation in polluted environments, ***Environ. Sci. Technol.***, 8, 4227–4242, https://doi.org/10.1021/acs.est.0c06496, 2021.

Liu, X. X., Zhang, Y., Huey, L. G., Yokelson, R. J., Wang, Y., Jimenez, J. L., Campuzano-Jost, P., Beyersdorf, A. J., Blake, D. R., Choi, Y., St Clair, J. M., Crounse, J. D., Day, D. A., Diskin, G. S., Fried, A., Hall, S. R., Hanisco, T. F., King, L. E., Meinardi, S., Mikoviny, T., Palm, B. B., Peischl, J., Perring, A. E., Pollack, I. B., Ryerson, T. B., Sachse, G., Schwarz, J. P., Simpson, I. J., Tanner, D. J., Thornhill, K. L., Ullmann, K., Weber, R. J., Wennberg, P. O., Wisthaler, A., Wolfe, G. M., and Ziemba, L. D.: Agricultural fires in the southeastern U.S. during SEAC^{4}RS: emissions of trace gases and particles and evolution of ozone, reactive nitrogen, and organic aerosol, ***J. Geophys. Res. Atmos.***, 121, 7383–7414, https://doi.org/10.1002/2016JD025040, 2016.

McClure, C. D., Lim, C. Y., Hagan, D. H., Kroll, J. H., and Cappa, C. D.: Biomass-burning-derived particles from a wide variety of fuels – Part 1: properties of primary particles, ***Atmos. Chem. Phys.***, 20, 1531–1547, https://doi.org/10.5194/acp-20-1531-2020, 2020.

637 McMeeking, G. R., Kreidenweis, S. M., Baker, S., Carrico, C. M., Chow, J. C., Collett Jr., J. L.,
638 Hao, W. M., Holden, A. S., Kirchstetter, T. W., Malm, W. C., Moosmüller, H., Sullivan, A. P.,
639 and Wold, C. E.: Emissions of trace gases and aerosols during the open combustion of biomass
640 in the laboratory, ***J. Geophys. Res.***, 114, D19210, https://doi.org/10.1029/2009JD011836, 2009.

641 Mohr, C., Lopez-Hilfiker, F. D., Zotter, P., Prévôt, A. S. H., Xu, L., Ng, N. L., Herndon, S. C.,
642 Williams, L. R., Franklin, J. P., Zahniser, M. S., Worsnop, D. R., Knighton, W. B., Aiken, A.
643 C., Gorkowski, K. J., Dubey, M. K., Allan, J. D., and Thornton, J. A.: Contribution of nitrated
644 phenols to wood burning brown carbon light absorption in Detling, United Kingdom during
645 winter time, ***Environ. Sci. Technol.***, 47, 6316–6324, https://doi.org/10.1021/es400683v, 2013.

646 Ni, H. Y., Huang, R. J., Pieber, S. M., Corbin, J. C., Stefenelli, G., Pospisilova, V., Klein, F., Gysel-
647 Beer, M., Yang, L., Baltensperger, U., El Haddad, I., Slowik, J. G., Cao, J. J., Prévôt, A. S. H.,
648 and Dusek, U.: Brown carbon in primary and aged coal combustion emission, ***Environ. Sci.***
649 ***Technol.,*** 55, 5701–5710, https://doi.org/10.1021/acs.est.0c08084, 2021.

650 Pokhrel, R. P., Wagner, N. L., Langridge, J. M., Lack, D. A., Jayarathne, T., Stone, E. A., Stockwell,
651 C. E., Yokelson, R. J., and Murphy, S. M.: Parameterization of single-scattering albedo (SSA)
652 and absorption Ångström exponent (AAE) with EC/OC for aerosol emissions from biomass
653 burning, ***Atmos. Chem. Phys.***, 16, 9549–9561, https://doi.org/10.5194/acp-16-9549-2016,
654 2016.

655 Saleh, R.: From measurements to models: toward accurate representation of brown carbon in climate
656 calculations, ***Curr. Pollut. Rep.***, 6, 90–104, https://doi.org/10.1007/s40726-020-00139-3, 2020.

657 Salvador, C. M. G., Tang, R. Z., Priestley, M., Li, L. J., Tsiligiannis, E., Le Breton, M., Zhu, W. F.,
658 Zeng, L. M., Wang, H., Yu, Y., Hu, M., Guo, S., and Hallquist, M.: Ambient nitro-aromatic
659 compounds – biomass burning versus secondary formation in rural China, ***Atmos. Chem. Phys.***,
660 21, 1389–1406, https://doi.org/10.5194/acp-21-1389-2021, 2021.

661 Sand, M., Samset, B. H., Myhre, G., Gliβ, J., Bauer, S. E., Bian, H. S., Chin, M., Checa-Garcia, R.,
662 Ginoux, P., Kipling, Z., Kirkevåg, A., Kokkola, H., Le Sager, P., Lund, M. T., Matsui, H., van
663 Noije, T., Olivié, D. J. L., Remy, S., Schulz, M., Stier, P., Stjern, C. W., Takemura, T., Tsigaridis,
664 K., Tsyro, S. G., and Watson-Parris, D.: Aerosol absorption in global models from AeroCom
665 phase III, ***Atmos. Chem. Phys.***, 21, 15929–15947, https://doi.org/10.5194/acp-21-15929-2021,
666 2021.

667 Shen, X. B., Hao, J. T., Kong, L., Shi, Y., Cao, X. Y., Shi, J. C., Yao, Z. L., Li, X., Wu, B. B., Xu, Y.
668 M., and He, K. B.: Variation characteristics of fine particulate matter and its components in
669 diesel vehicle emission plumes, ***J. Environ. Sci.***, 107, 138–149,
670 https://doi.org/10.1016/j.jes.2021.01.034, 2021.

Su, H., Cheng, Y. F., and Pöschl, U.: New multiphase chemical processes influencing atmospheric aerosols, air quality, and climate in the Anthropocene, ***Acc. Chem. Res.***, 53, 2034–2043, https://doi.org/10.1021/acs.accounts.0c00246, 2020.

Tabazadeh, A., Djikaev, Y. S., and Reiss, H.: Surface crystallization of supercooled water in clouds, ***Proc. Natl. Acad. Sci. USA***, 99, 15873–15878, https://doi.org/10.1073/pnas.252640699, 2002.

Wang, Q. Q., Zhou, Y. Y., Ma, N., Zhu, Y., Zhao, X. C., Zhu, S. W., Tao, J. C., Hong, J., Wu, W. J., Cheng, Y. F., and Su, H.: Review of brown carbon aerosols in China: pollution level, optical properties, and emissions, ***J. Geophys. Res. Atmos.***, 127, e2021JD035473, https://doi.org/10.1029/2021JD035473, 2022.

Wang, Y. S., Li, W. J., Gao, W. K., Liu, Z. R., Tian, S. L., Shen, R. R., Ji, D. S., Wang, S., Wang, L. L., Tang, G. Q., Song, T., Cheng, M. T., Wang, G. H., Gong, Z. Y., Hao, J. M., and Zhang, Y. H.: Trends in particulate matter and its chemical compositions in China from 2013-2017, ***Sci. China Earth Sci.***, 62, 1857–1871, https://doi.org/10.1007/s11430-018-9373-1, 2019.

Washenfelder, R. A., Azzarello, L., Ball, K., Brown, S. S., Decker, Z. C. J., Franchin, A., Fredrickson, C. D., Hayden, K., Holmes, C. D., Middlebrook, A. M., Palm, B. B., Pierce, R. B., Price, D. J., Roberts, J. M., Robinson, M. A., Thornton, J. A., Womack, C. C., and Young, C. J.: Complexity in the evolution, composition, and spectroscopy of brown carbon in aircraft measurements of wildfire plumes, ***Geophys. Res. Lett.***, 49, e2022GL098951, https://doi.org/10.1029/2022GL098951, 2022.

Wozniak, A. S., Bauer, J. E., Sleighter, R. L., Dickhut, R. M., and Hatcher, P. G.: Technical Note: Molecular characterization of aerosol-derived water soluble organic carbon using ultrahigh resolution electrospray ionization Fourier transform ion cyclotron resonance mass spectrometry, ***Atmos. Chem. Phys.***, 8, 5099–5111, https://doi.org/10.5194/acp-8-5099-2008, 2008.

Wu, J., Kong, S. F., Yan, Y. Y., Yao, L. Q., Yan, Q., Liu, D. T., Shen, G. F., Zhang, X. Y., and Qi, S. H.: Neglected biomass burning emissions of air pollutants in China-views from the corncob burning test, emission estimation, and simulations, ***Atmos. Environ.***, 278, 119082, https://doi.org/10.1016/j.atmosenv.2022.119082, 2022.

Xie, M. J., Chen, X., Hays, M. D., and Holder, A. L.: Composition and light absorption of N-containing aromatic compounds in organic aerosols from laboratory biomass burning, ***Atmos. Chem. Phys.***, 19, 2899–2915, https://doi.org/10.5194/acp-19-2899-2019, 2019.

Xie, M. J., Zhao, Z. Z., Holder, A. L., Hays, M. D., Chen, X., Shen, G. F., Jetter, J. J., Champion, W. M., and Wang, Q. G.: Chemical composition, structures, and light absorption of N-containing aromatic compounds emitted from burning wood and charcoal in household

cookstoves, ***Atmos. Chem. Phys.***, 20, 14077–14090, https://doi.org/10.5194/acp-20-14077-2020, 2020.

Xu, J. Z., Hettiyadura, A. P. S., Liu, Y. M., Zhang, X. H., Kang, S. C., and Laskin, A.: Atmospheric brown carbon on the Tibetan Plateau: regional differences in chemical composition and light absorption properties, ***Environ. Sci. Technol. Lett.***, 9, 219−225, https://doi.org/10.1021/acs.estlett.2c00016, 2022.

Yang, M., Howell, S. G., Zhuang, J., and Huebert, B. J.: Attribution of aerosol light absorption to black carbon, brown carbon, and dust in China - Interpretations of atmospheric measurements during EAST-AIRE, ***Atmos. Chem. Phys.***, 9, 2035–2050, https://doi.org/10.5194/acp-9-2035-2009, 2009.

Yttri, K. E., Schnelle-Kreis, J., Maenhaut, W., Abbaszade, G., Alves, C., Bjerke, A., Bonnier, N., Bossi, R., Claeys, M., Dye, C., Evtyugina, M., Garc á-Gacio, D., Hillamo, R., Hoffer, A., Hyder, M., Iinuma, Y., Jaffrezo, J. L., Kasper-Giebl, A., Kiss, G., Lopez-Mahia, P. L., Pio, C., Piot, C., Ramirez-Santa-Cruz, C., Sciare, J., Teinil ä, K., Vermeylen, R., Vicente, A., and Zimmermann, R.: An intercomparison study of analytical methods used for quantification of levoglucosan in ambient aerosol filter samples, ***Atmos. Meas. Tech.***, 8, 125–147, https://doi.org/10.5194/amt-8-125-2015, 2015.

Yuan, Q., Qi, B., Hu, D. Y., Wang, J. J., Zhang, J., Yang, H. Q., Zhang, S. S., Liu, L., Xu, L., and Li, W. J.: Spatiotemporal variations and reduction of air pollutants during the COVID-19 pandemic in a megacity of Yangtze River Delta in China, ***Sci. Total Environ.***, 751, 141820, https://doi.org/10.1016/j.scitotenv.2020.141820, 2021.

Zeng, L. H., Dibb, J., Scheuer, E., Katich, J. M., Schwarz, J. P., Bourgeois, I., Peischl, J., Ryerson, T., Warneke, C., Perring, A. E., Diskin, G. S., DiGangi, J. P., Nowak, J. B., Moore, R. H., Wiggins, E. B., Pagonis, D., Guo, H. Y., Campuzano-Jost, P., Jimenez, J. L., Xu, L., and Weber, R. J.: Characteristics and evolution of brown carbon in western United States wildfires, ***Atmos. Chem. Phys.***, 22, 8009–8036, https://doi.org/10.5194/acp-22-8009-2022, 2022.

Zeng, L. H., Zhang, A. X., Wang, Y. H., Wagner, N. L., Katich, J. M., Schwarz, J. P., Schill, G. P., Brock, C., Froyd, K. D., Murphy, D. M., Williamson, C. J., Kupc, A., Scheuer, E., Dibb, J., and Weber, R. J.: Global measurements of brown carbon and estimated direct radiative effects, ***Geophys. Res. Lett.***, 47, e2020GL088747, https://doi.org/10.1029/2020GL088747, 2020.

Zeng, Y. L., Ning, Y. L., Shen, Z. X., Zhang, L. M., Zhang, T., Lei, Y. L., Zhang, Q., Li, G. H., Xu, H. M., Ho, S. S. H., and Cao, J. J.: The roles of N, S, and O in molecular absorption features of brown carbon in $PM_{2.5}$ in a typical semi-arid megacity in Northwestern China, ***J. Geophys. Res. Atmos.***, 126, e2021JD034791, https://doi.org/10.1029/2021JD034791, 2021.

739 Zhang, J., Smith, K. R., Ma, Y., Ye, S., Jiang, F., Qi, W., Liu, P., Khalil, M. A. K., Rasmussen, R.
740 A., and Thorneloe, S. A.: Greenhouse gases and other airborne pollutants from household
741 stoves in China: a database for emission factors, ***Atmos. Environ.***, 34, 4537–4549,
742 https://doi.org/10.1016/S1352-2310(99)00450-1, 2000.

743 Zhang, Y. L., Wang, X. M., Li, G. H., Yang, W. Q., Huang, Z. H., Zhang, Z., Huang, X. Y., Deng,
744 W., Liu, T. Y., Huang, Z. Z., and Zhang, Z. Y.: Emission factors of fine particles, carbonaceous
745 aerosols and traces gases from road vehicles: recent tests in an urban tunnel in the Pearl River
746 Delta, China, ***Atmos. Environ.***, 122, 876–884, https://doi.org/10.1016/j.atmosenv.2015.08.024,
747 2015.

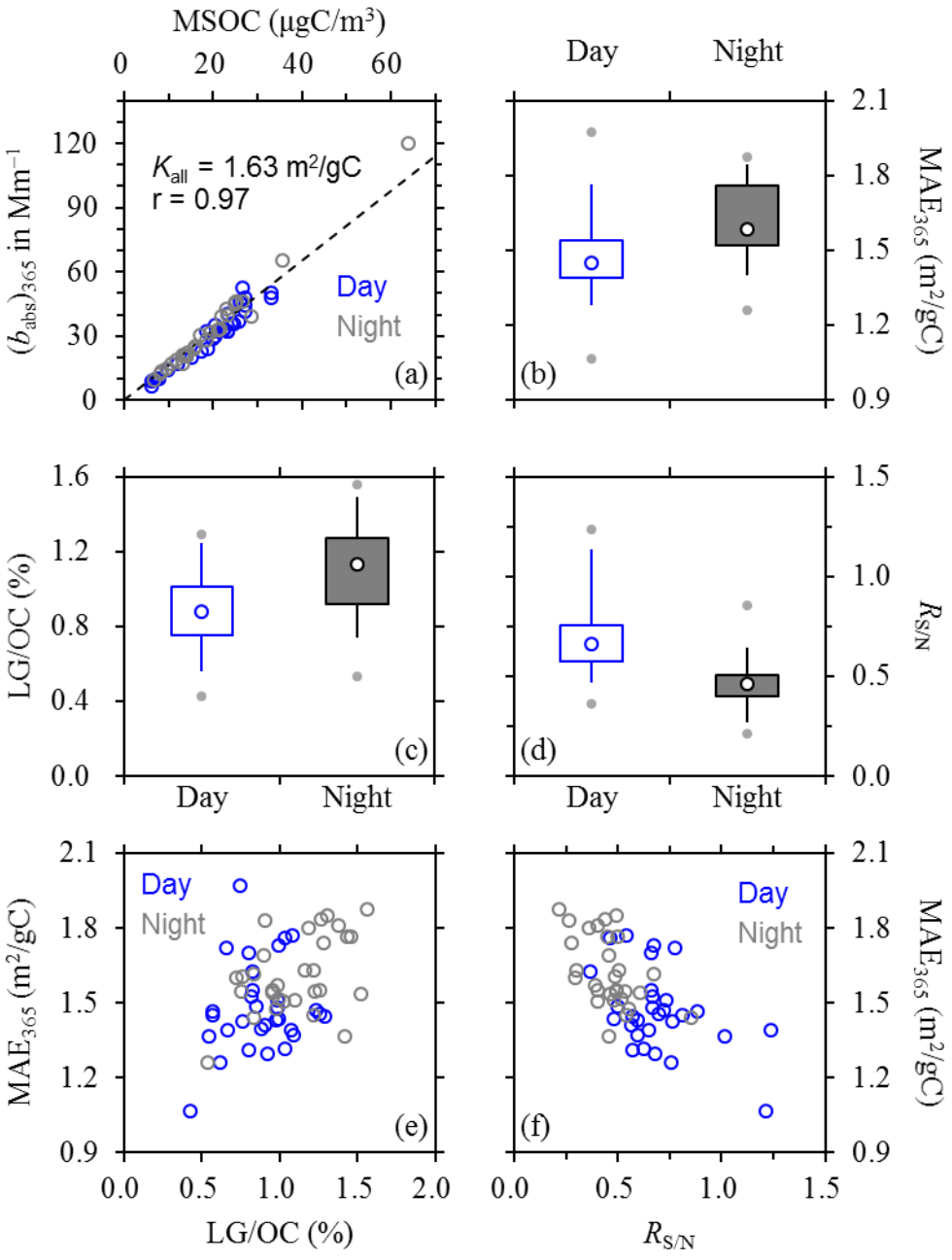

748

749 **Figure 1. (a)** Dependence of $(b_{abs})_{365}$ on MSOC, **(b–d)** diurnal variations of MAE_{365}, LG/OC (on a
750 basis of carbon mass) and $R_{S/N}$, and **(e–f)** dependences of MAE_{365} on LG/OC or $R_{S/N}$ during winter.
751 In (a), the dashed line indicates linear regression result based on all the winter samples, with K_{all} as
752 slope (intercept was set as zero). In (b-d), lower and upper box bounds indicate the 25th and 75th
753 percentiles, the whiskers below and above the box indicate the 5th and 95th percentiles, the solid
754 circles below and above the box indicate the minimum and maximum, and the open circle within
755 the box marks the median (the same hereinafter). Comparison of (e) and (f) suggests that the
756 wintertime MAE_{365} was more strongly influenced by $R_{S/N}$ compared to LG/OC. The dependence
757 shown in (f) could be approximated by the following function for all the winter samples (r = 0.61):
758 $MAE_{365} = (-0.51 \pm 0.09) \times R_{S/N} + (1.84 \pm 0.05)$.

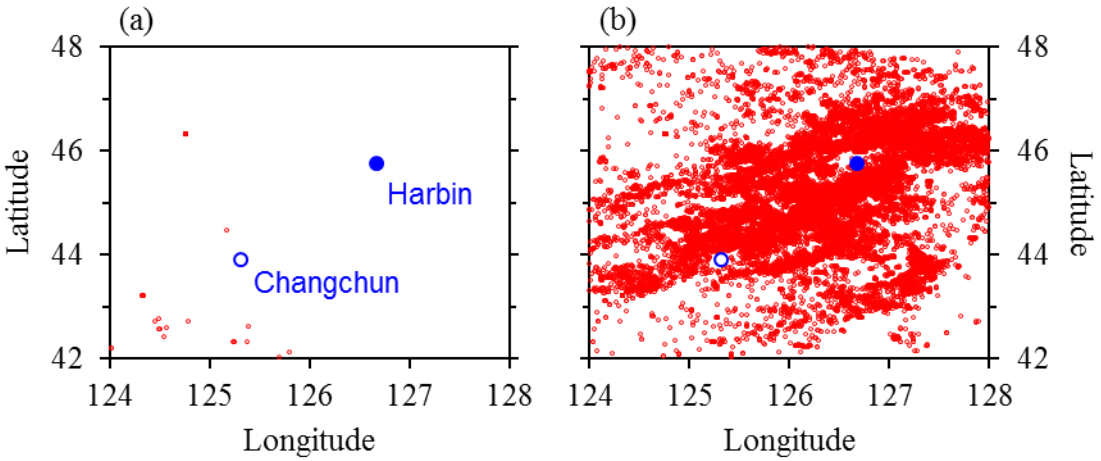

Figure 2. Cumulative fire hotspots detected throughout the **(a)** winter and **(b)** spring measurement periods around Harbin, with their locations shown by the red circles. The HC metropolitan area has two central cities as marked by the blue circles. The fire data were based on the joint NASA/NOAA Suomi National Polar-orbiting Partnership (S-NPP) satellite, and were downloaded from the Fire Information for Resource Management System (FIRMS; https://firms.modaps.eosdis.nasa.gov/, last access: 1 January, 2023).

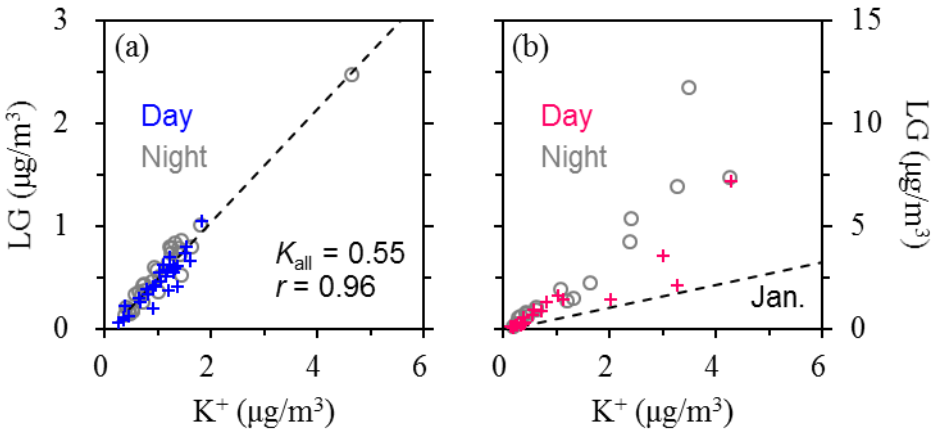

Figure 3. Dependences of levoglucosan on K^+ during **(a)** winter and **(b)** spring. In (a), the dashed line indicates linear regression result based on all the winter samples, with K_{all} as slope. The regression line of winter campaign is also shown in (b) for comparison to highlight the increased and variable LG/K^+ ratios in spring. The relatively low and constant LG/K^+ in winter were attributed to residential burning of crop residues, a routine activity occurring every day in rural areas for cooking and heating. The higher LG/K^+ in spring were associated with agricultural fires, as supported by the intensive fire hotspots detected.

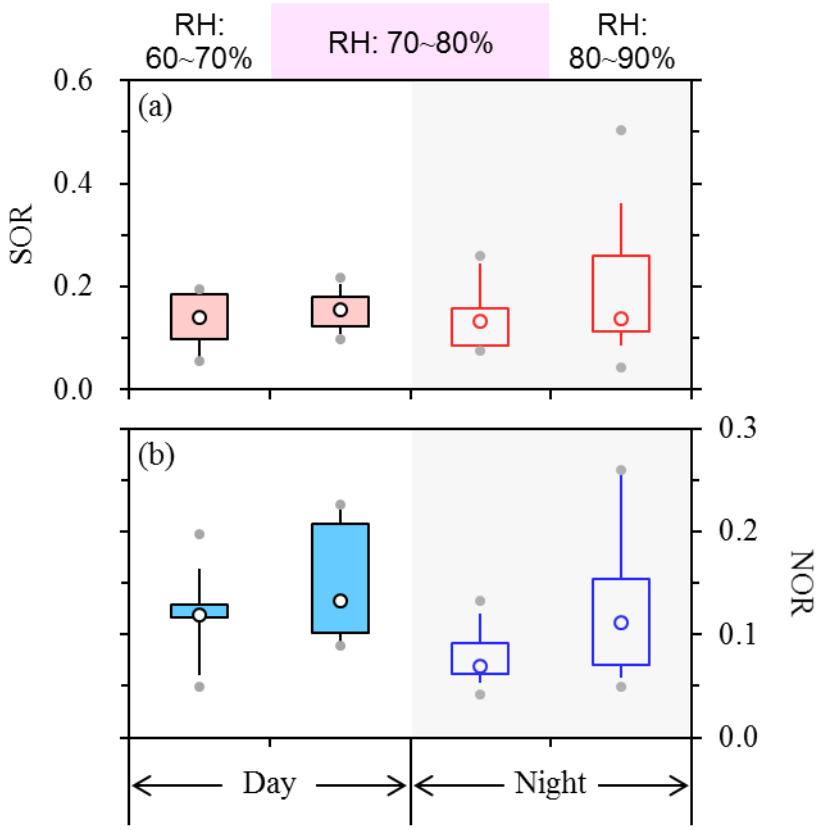

774

775 **Figure 4.** Diurnal variations of **(a)** SOR and **(b)** NOR in winter, with results from different RH
776 ranges shown separately. Daytime and nighttime samples had a common RH range of 70–80%,
777 whereas low RH levels of 60–70% and high RH levels of 80–90% occurred only during the day and
778 at night, respectively.

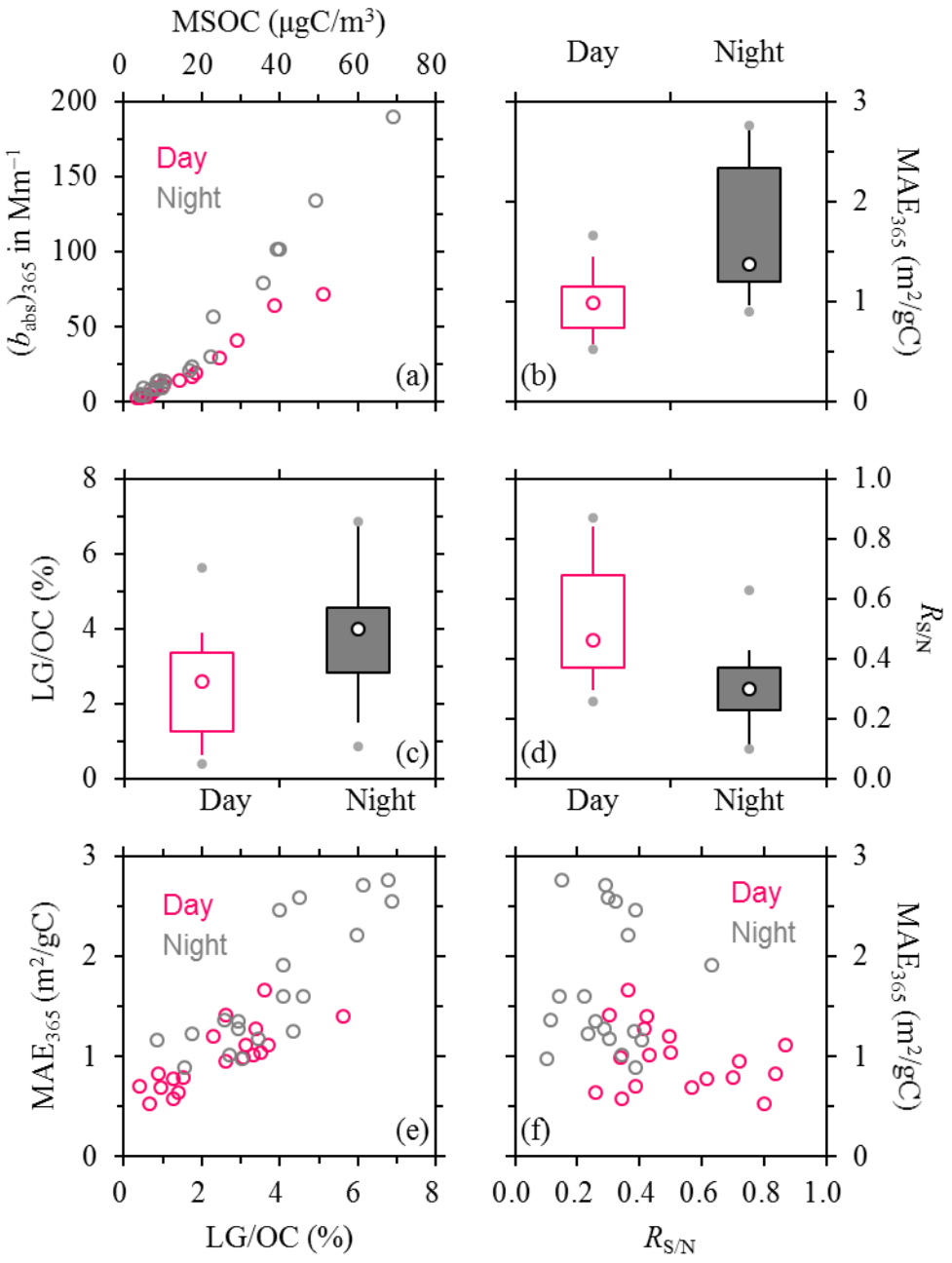

779

780 **Figure 5.** The same as Figure 1 but for spring. MAE_{365} showed more pronounced diurnal variations
781 in spring than winter, although the daytime vs. nighttime discrepancies in $R_{S/N}$ were comparable
782 between the two seasons. Comparison of (e) and (f) suggests that unlike winter, the springtime
783 MAE_{365} was more strongly influenced by LG/OC than by $R_{S/N}$. The dependence shown in (e) could
784 be approximated by the following function for all the spring samples (r = 0.84): MAE_{365} = (30.48 ±
785 3.28) × LG/OC + (0.39 ± 0.12), where LG/OC is on a basis of carbon mass and in %.

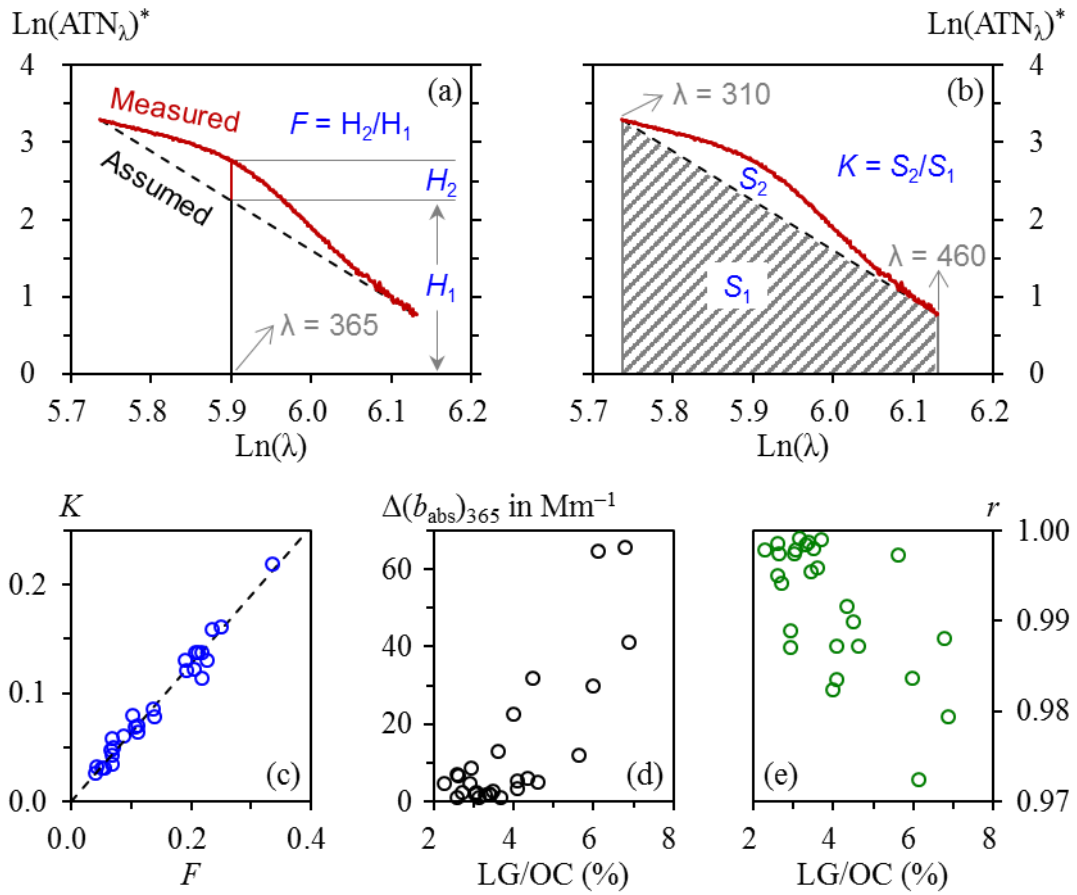

786

787 **Figure 6.** Nonlinearity of $\ln(ATN_\lambda)^*$ on ln (λ) during agricultural fire episodes in spring: **(a–b)**
788 illustrations of the determination of *F* and *K*, **(c)** comparison of *K* and *F*, and **(d–e)** dependences of
789 $\Delta(b_{abs})_{365}$ and *r* on LG/OC. In (a) and (b), the measured spectrum correspond to the nighttime sample
790 collected on April 21, 2021, which had an LG/OC of 6.87%; the assumed spectrum was generated
791 by drawing a line between the two points with *x* values of ln(310) and ln(460); H_1 indicates
792 $\ln(ATN_{365})^*$ of the assumed spectrum, while H_2 indicates the difference in $\ln(ATN_{365})^*$ between the
793 two spectra; S_1 indicates the area enclosed by the assumed spectrum and the *x*-axis, while S_2
794 indicates the area enclosed between the two spectra. In (c), the dashed line indicates linear regression
795 result (intercept was set as zero) and the corresponding *r* value was 0.99. In (e), *r* was derived from
796 linear regression of $\ln(ATN_\lambda)^*$ on ln (λ). Although the *r* values seemed reasonable, the AAE results
797 should be interpreted with caution given the apparent absorption peak at ~365 nm.

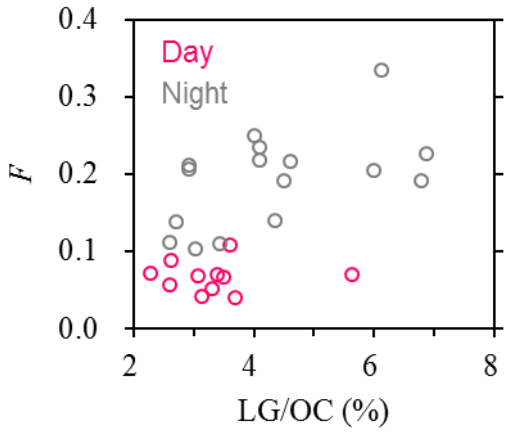

Figure 7. Dependence of *F*, a measure of the significance of the ~365 nm absorption peak, on LG/OC during agricultural fire episodes in spring. For a given LG/OC range, *F* decreased substantially during the day, likely due to photo-bleaching of chromophores associated with the ~365 nm peak. The same conclusion could be reached based on *K*, another indicator for the significance of the ~365 nm peak.